Appl Phys B (2010) 100: 159–168
DOI 10.1007/s00340-010-3985-y

Applied Physics B
Lasers and Optics

FDTD modeling of realistic semicontinuous metal films

U.K. Chettiar · P. Nyga · M.D. Thoreson · A.V. Kildishev · V.P. Drachev · V.M. Shalaev

Received: 1 March 2010 / Published online: 28 March 2010

Abstract We have employed a parallelized 3D FDTD (finite-difference time-domain) solver to study the electromagnetic properties of random, semicontinuous, metal films. The structural features of the simulated geometries are exact copies of the fabricated films and are obtained from SEM images of the films themselves. The simulation results show good agreement with the experimentally observed far-field spectra, allowing us to also study the nonlinear moments of the optical responses for these realistic nanostructures.

These results help to further our understanding of the details of the electromagnetic response of randomly structured metal films. Our results can also be applied in the optimization of random metal nanostructures and in the design of surface-enhanced spectroscopies and other plasmonic applications.

U.K. Chettiar (✉) · P. Nyga · M.D. Thoreson · A.V. Kildishev · V.P. Drachev · V.M. Shalaev
Birck Nanotechnology Center, School of Electrical and Computer Engineering, Purdue University, West Lafayette, IN, USA
e-mail: chettiar@seas.upenn.edu

P. Nyga
e-mail: pnyga@purdue.edu

M.D. Thoreson
e-mail: mthoreso@purdue.edu

A.V. Kildishev
e-mail: kildishev@purdue.edu

V.P. Drachev
e-mail: vdrachev@purdue.edu

V.M. Shalaev
e-mail: shalaev@purdue.edu

U.K. Chettiar
Department of Electrical and Systems Engineering, University of Pennsylvania, Philadelphia, PA, USA

P. Nyga
Institute of Optoelectronics, Military University of Technology, Warsaw, Poland

M.D. Thoreson
Graduate School for Advanced Optical Technologies (SAOT), Universität Erlangen-Nürnberg, Erlangen, Germany

1 Introduction

Much of the recent work on simulating complex metal–dielectric structures has been focused in one of two categories. Many metal–dielectric systems are periodic or exhibit a known geometry; these structures are studied numerically using finite-element methods, finite-difference methods, or even analytical methods in some cases. The other category for numerical simulations of metal–dielectric composites centers on modeling the system properties using macroscopic parameters that are relatively easy to obtain, such as the use of volume filling fractions and constituent permittivities in Bruggeman's effective medium theory (EMT) [1]. Unfortunately, neither of these categories of numerical simulation approaches is directly applicable to random metal–dielectric structures with strongly interacting metallic elements. This is due to the fact that simple models such as EMT do not take into account metal-particle interactions and therefore fail to properly predict important aspects of the film response, such as absorptance. While full-wave simulations such as FDTD would predict these responses properly, such numerical methods require a known geometry. Such exact geometries of random metal–dielectric films are essentially impossible to predict before fabrication. In this work,

we have taken a hybrid approach to simulating the electromagnetic response of semicontinuous metal films (SMFs), which are composed of a random metal film deposited on a dielectric substrate. These SMFs are random, fractal-type [2] metal–dielectric composites with nanometer-sized metallic structures and are sometimes referred to as percolation films. Such films consist of clusters and elongated islands of metal that resonate in a broad spectral range, extending from the UV into the near-IR and beyond [3, 4]. SMFs exhibit unusual optical and electrical properties that are significantly different from the constituent materials. Such materials can show interesting properties near the percolation threshold, which is defined as the metal filling fraction where the conductivity of the film undergoes a transition from being dielectric in nature to metallic in nature. One of the most remarkable properties of such composite films is the localization and large enhancement of electric and magnetic fields in the visible and infrared spectral ranges [5, 6]. Substances placed in the vicinity of the films experience dramatically enhanced optical responses in a broad spectral range that can extend from the visible to the infrared spectral region. Films such as SMFs can be used for surface-enhanced Raman and infra-red absorption spectroscopies (SERS [7–11], SEIRA [12–15]) with extremely high sensitivities capable of monolayer molecular spectroscopy. Semicontinuous metal films can also be used in solar cells [16, 17] or for developing novel optical elements such as optical filters with transparency windows that can be controlled by local photo-modification in the composite films [18, 19].

Metal-dielectric composites are typically fabricated by depositing metal vapor onto a dielectric substrate. At low metal concentrations, the film consists of mutually separated grains of metal with sizes of the order of tens of nanometers. As the metal filling fraction increases, the metal grains start to coalesce together to form irregular fractal-like structures. At a particular metal concentration called the percolation threshold (p_c) the metal particles combine together to create an infinite metal cluster that forms a continuous path across the sample. Hence, the percolation threshold marks a dielectric-to-metal phase transition [20]. At even higher metal concentrations, the film becomes mostly metallic with dielectric voids that will finally vanish through additional metal deposition to eventually produce a uniform metal film. The dependence of SMF electrical resistance as a function of the filling fraction (p) was discussed in [21].

The optical properties of thin noble metal films also strongly depend on their local nanostructure. The unique geometrical properties of metal films near the percolation threshold lead to localized surface plasmons and localization of strongly enhanced electromagnetic fields in regions called "hot spots" [22–24]. The electromagnetic energy density in the hot spots can exceed the incident energy density by up to 10^5 [5].

Due to the enormous complexity of the problem, the numerical studies of semicontinuous films in the past were limited to mean field theories [1, 25], quasi-static approximations [5, 6] or other approximations like lumped-circuit models [6]. For linear problems, predictions from Bruggeman's effective medium theory [1] are usually sensible physically and offer quick insight into problems that are difficult to approach by other means. However, the effective medium theory has a disadvantage that is typical of all mean field theories—it diminishes the role of fluctuations in a system.

In this paper we have employed a parallelized 3D FDTD (finite-difference time-domain) solver to study the electromagnetic properties of semicontinuous metal films without any approximations except for the discrete nature of the method. Moreover, the structural features of the simulated geometries are exact copies of the realistic films and are obtained from SEM images. This enables direct comparisons against computer-generated random structures and against the predictions from an EMT-based analysis. In addition to simulating the linear electromagnetic properties of the composites, we have also studied the nonlinear moments of optical responses, which are also calculated for realistic nanostructures.

2 Semicontinuous metal films

2.1 Fabrication

Silver films of various thicknesses were deposited on glass substrates (microscope slides, Erie Scientific) at room temperature using an electron-beam vacuum evaporation system (CHA Industries Model 600, modified in-house). Shortly before the evaporation process, the glass substrates were submerged in piranha (H_2O:$2H_2SO_4$) bath for 20 minutes and were then rinsed with ultrapure water. Next the substrates were rigorously rinsed multiple times with methanol, isopropyl alcohol and acetone and dried with gaseous nitrogen. The substrates were then loaded into the e-beam system whose initial pressure inside the vacuum chamber was approximately 10^{-6} Torr. The film thickness and deposition rate were monitored with a quartz crystal oscillator. The silver deposition rate for all the samples was kept at 0.05 nm s^{-1}. Silver from Alfa Aesar (99.9999% purity) was used as a source material. An intermediate layer of silicon dioxide (SiO_2, Kurt J. Lesker Company, 99.999% purity) was deposited prior to the metal in the same evaporation process. The fabricated samples were stored in a dry N_2 environment for up to several weeks prior to characterization or further studies.

2.2 Characterization

The fabricated films were characterized with a field-emission scanning electron microscope (FESEM, Hitachi S-4800) in

order to determine the metal nanostructure. The metal coverage ratio of each film was calculated from the FESEM images. The transmittance of the films at normal incidence was measured with a Lambda 950 spectrophotometer (Perkin Elmer) in the 0.3–2.5 μm wavelength range. The reflectance of the films was measured at 8° incidence in the 0.3–2.5 μm wavelength range using a 150 mm integrating sphere accessory and the spectrophotometer. The wavelength step size for both transmittance and reflectance measurements was set at 5 nm.

2.3 Simulations

As mentioned above, a parallelized 3D FDTD solver [26] was employed to study the electromagnetic properties of the nanostructured metal films. The permittivity of silver was modeled using the Drude equation with parameters obtained from experimental results [27]. The FDTD results were compared with the Bruggeman effective medium theory (EMT) [1] and experimentally measured data. The EMT predicts that the local electric field should be the same in all metal grains regardless of their local arrangement in a composite. Therefore, the local field is predicted in EMT to be almost uniform even near the percolation threshold. This is counterintuitive since percolation represents a phase transition where one would expect fluctuations to play a crucial role in determining the system's physical properties [5]. According to the Bruggeman EMT, the effective permittivity (ε_e) of a d-dimensional metal–dielectric composite consisting of a metal with permittivity ε_m and filling fraction p and a dielectric with permittivity ε_d and filling fraction $(1-p)$ is given by (1). This is a quadratic equation which has two solutions for the effective permittivity ε_e. We select the solution that has a positive imaginary part ε_e''

$$p\frac{(\varepsilon_m-\varepsilon_e)}{[\varepsilon_m+(d-1)\varepsilon_e]}+(1-p)\frac{(\varepsilon_d-\varepsilon_e)}{[\varepsilon_d+(d-1)\varepsilon_e]}=0. \quad (1)$$

2.4 Experimental films

As mentioned above, the optical properties of thin noble metal films strongly depend on their nanostructure. The correlation between the fabricated silver film geometries and their transmittance, reflectance and absorptance spectra can be clearly seen in Figs. 1 and 2, respectively. The sample with a mass thickness of 7 nm has a distinct absorptance band in the visible, centered at about 500 nm (this corresponds to a dip in transmittance). This band extends well into the infrared part of the spectrum. The transmittance of the film reaches almost that of the bare glass substrate at a wavelength slightly above 2 μm. For the longer wavelengths, the film is highly transparent. The source of such an optical response lies in the film's metal structure. The

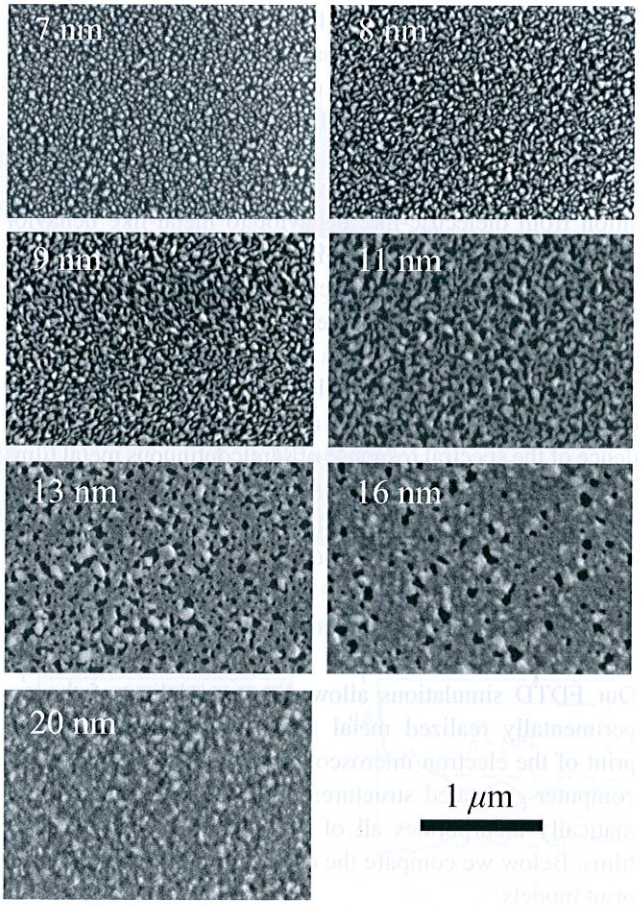

Fig. 1 FESEM image of semicontinuous silver films at various equivalent mass thicknesses

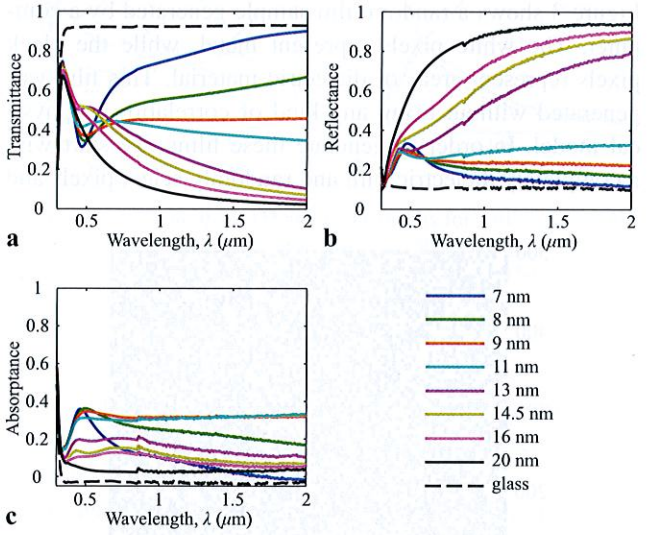

Fig. 2 Transmittance, reflectance and absorptance of SMFs with various equivalent mass thicknesses

film consists of densely packed silver particles with various sizes and shapes that are mostly spheroidal with low aspect ratios. Such structures have plasmon resonances in the

visible and the near-IR. For films with higher silver mass thicknesses, the shape of metal particles becomes more irregular, and the particles start connecting and forming small fractals. The transmittance of these films decreases, especially at longer wavelengths, as a result of an increase in both reflectance and absorptance. The film undergoes a transition from dielectric-like behavior to metal-like behavior at a silver thickness somewhere between 9 and 11 nm. These two samples show spectral properties that are almost wavelength-independent in the measured range. With the addition of more metal, the film structure becomes more continuous; the reflectance quickly increases, resulting in a decrease in both transmittance and absorptance. The dependence of the spectral response of semicontinuous metal films on the structure and mass thickness were studied previously by many groups and have been extensively reported [28–31].

3 Simulation results and discussion

Our FDTD simulations allow direct modeling of the experimentally realized metal nanostructures using a footprint of the electron microscopy images. In contrast to any computer-generated structures, the footprint method automatically incorporates all of the details of the fabricated films. Below we compare the computer-generated and footprint models.

3.1 Simulations with computer-generated films

Figure 3 shows a random film sample generated by a computer. The white pixels represent metal, while the black pixels represent areas of dielectric material. This film was generated without using any kind of correlation or physical model. In order to generate these films, we start with a completely dielectric film and randomly select pixels and convert them to metal. This process is continued until the desired metal filling-fraction is reached. Consequently, we see significant differences between the metal structure of the computer-generated film and the actual film. Because of the differences, we expect that the computer-generated film will not produce a simulated local-field distribution that is completely consistent with the real semicontinuous metal film.

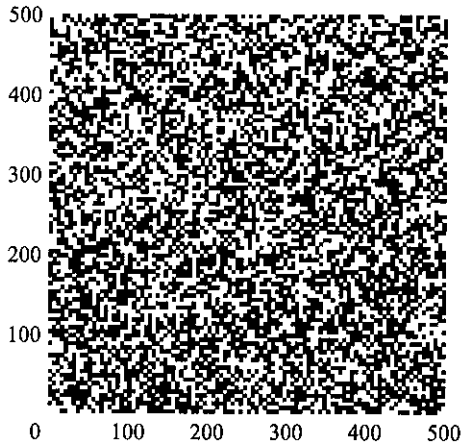

Fig. 3 A sample computer-generated random film where the surface coverage is 50%. The *axis* shows the length in nm

In Fig. 4 we show the local intensity enhancements obtained from FDTD simulations for a computer-generated silver film on a glass substrate with a surface coverage as shown in Fig. 3. The height of all the silver particles was set at 20 nm, and the particles were modeled with vertical sidewalls. The results of the FDTD simulations show huge local-field intensity enhancements, up to a few thousand times the incident field intensity. This figure is in agreement with published values [5]. These huge local-field intensities enhance the nonlinear response of these films, making the films very attractive for the large number of previously mentioned applications.

In order to obtain a comparison with EMT, we simulated multiple realizations of random films with the same filling fraction and averaged the spectra of all the realizations to get an overall spectral response. Figure 5 shows the results obtained by averaging the results of four individual realizations. As before, the film was a 20 nm-thick silver-air composite with a 50% metal filling fraction. The light green lines show the results of the individual realizations, and the dark solid lines show the average. The dashed line shows the results predicted by EMT. As seen in the figure, our averaged FDTD simulation results agree very well with EMT.

In Fig. 6 we show the comparison between our FDTD and EMT results for various filling fractions. As we saw before, the agreement is very good for a metal filling fraction of 50%, which corresponds to the theoretical percolation threshold for our thin film composites. However, the agreement between EMT and FDTD progressively worsens as the filling fraction moves away from 50%. Figure 6 shows that our FDTD simulations in general predict a wider absorptance band than that predicted by EMT. At a 50% filling fraction, both EMT and FDTD predict a very wide absorptance band, as is expected at the percolation threshold. However, as the filling fraction deviates from the percolation threshold, the EMT model predicts a narrower absorptance band with a very well-defined and sharp edge. In contrast, our FDTD simulations predict a wider absorptance band with a smooth edge and are therefore consistent with other numerical results [6]. This indicates a limitation on the applicability of EMT at filling fractions away from the percolation threshold.

3.2 Simulations with realistic films

As noted in the previous section, the computer-generated films do not accurately mimic the physical films that are

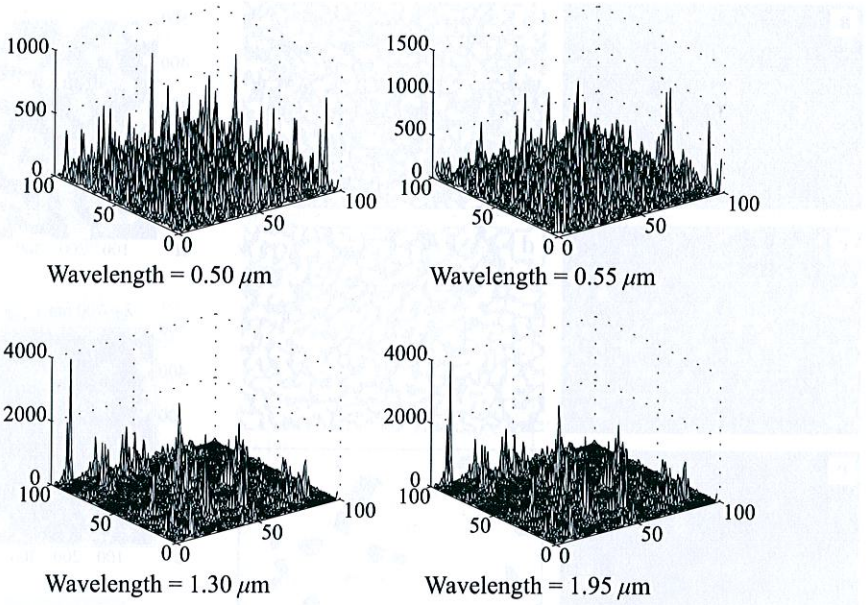

Fig. 4 Local intensity enhancement in the semicontinuous silver film at four different wavelengths

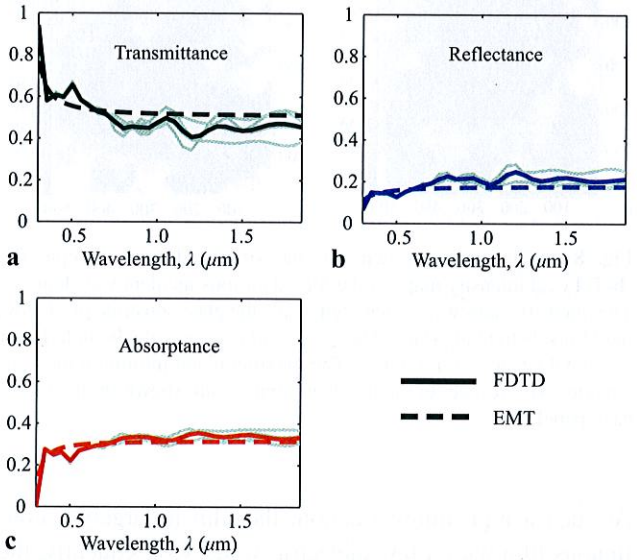

Fig. 5 The transmittance, reflectance and absorptance spectra for a 20 nm-thick silver dielectric composite with a 50% filling fraction. The results were obtained by averaging the results of 4 iterations. The *light green lines* show the results for individual iterations and the *solid lines* shows the average. The *dashed lines* show the result expected from EMT

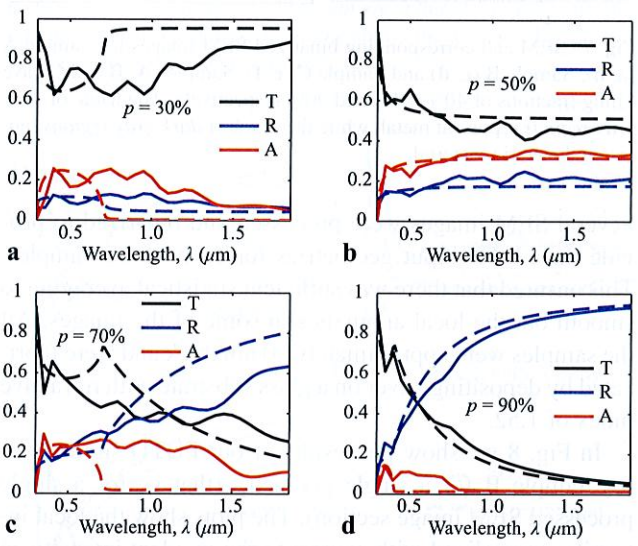

Fig. 6 Comparison of FDTD and EMT results for various silver filling fractions (p). (**a**) $p = 30\%$, (**b**) $p = 50\%$, (**c**) $p = 70\%$ and (**d**) $p = 90\%$. In all cases the film was 20 nm thick. The *solid lines* represent the FDTD results and *dashed lines* show the results predicted from EMT

fabricated using electron-beam deposition. Our computer-generated films are created using uncorrelated, random number sequences and do not incorporate any physics-based models to determine the aggregation effects that are expected in the growth of the actual films. Therefore, we would expect a copy or image of the experimental nanostructure to be a much better representation of the nanostructure for simulating the response of the physical films. Hence, we have used a number of SEM images of real films as inputs to our FDTD simulations. The SEM images were converted to binary (black/white) images using an appropriate threshold to distinguish the regions on the film that are occupied by metal from those that are dielectric.

We have studied three separate samples using this method. The samples, herein referred to as Samples A, B and C, correspond to the films presented in Figs. 1 and 2 with thicknesses of 8, 9 and 16 nm, respectively. The samples are presented in Fig. 7, where we show both the representative original SEM images and the processed and binarized images of the three samples. Samples A, B and C have metal filling fractions around 40%, 54% and 90%, respectively.

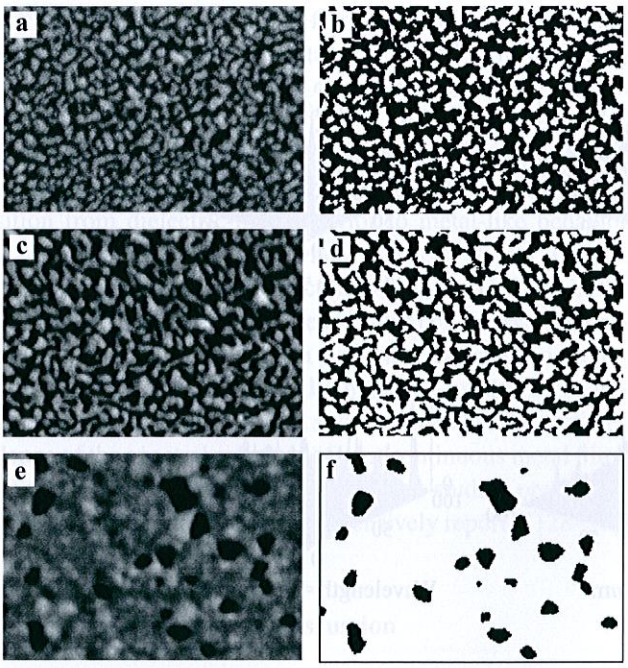

Fig. 7 SEM and corresponding binarized SEM images for Sample A (**a**, **b**), Sample B (**c**, **d**) and Sample C (**e**, **f**). Samples A, B and C have filling fractions of 40%, 54% and 90% respectively. The *white* or *light gray regions* represent metal, while the *black* or *dark gray regions* represent dielectric material

Several SEM images were processed and binarized to provide the FDTD input geometries for each of the samples. This ensured that there was sufficient statistical averaging to smooth out the local anomalies in some of the images. All the samples were approximately 20 nm thick and were fabricated by depositing silver on a glass substrate with refractive index of 1.52.

In Fig. 8 we show the results of our FDTD simulations for Sample B for a single geometry (that is, for a single processed SEM image section). The plots show the local intensity, normalized with respect to the incident intensity, at various incident wavelengths. The intensity map was calculated in a plane just inside the glass substrate and below the film/substrate interface. In the plots in Fig. 8, the maximum value of the color axis was set at 100 to improve clarity; the maximum and minimum local intensities and the wavelength are provided in the title of each plot. From the intensity maps, it is clear that the film shows large local-field enhancements for a wide range of wavelengths. This is typical of films near the percolation threshold as is the case with this film. Secondly, the regions in the film that provide the highest local enhancements vary with the wavelength. In other words, different regions in the film resonate at different wavelengths.

For Sample C, Fig. 9 shows the field intensity results from our simulations. As is clear from the geometry of Sample C, the sample has a very large metal filling fraction (~94%) and is well beyond the percolation threshold.

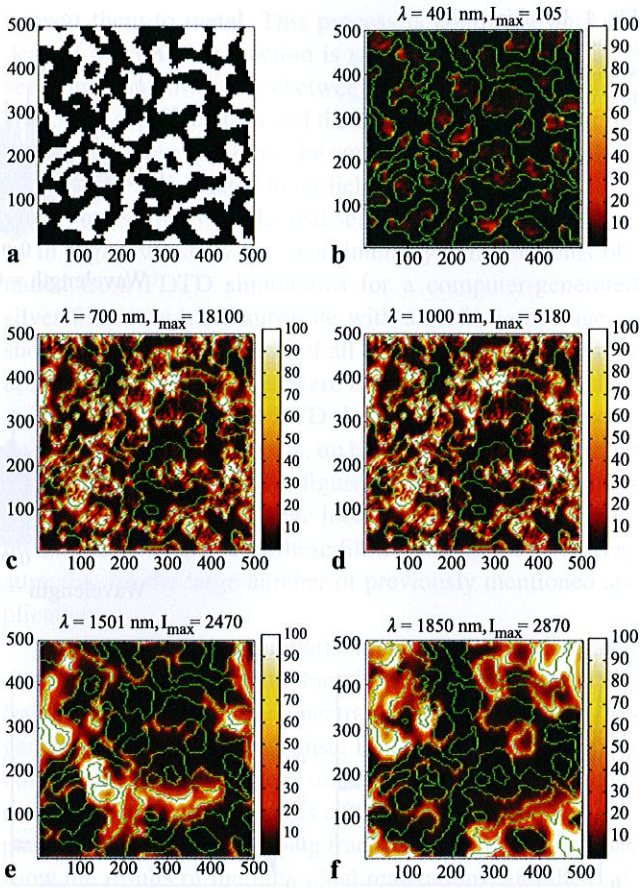

Fig. 8 (**a**) In-plane geometry of the simulated film (Sample B). (**b–f**) Local intensity maps of the film at various incident wavelengths. The intensity maps were calculated inside the glass substrate just below the film/substrate interface. The *green outlines* show the boundaries of the metal islands for reference. The maximum and minimum local intensities with respect to the incident intensity are shown in the title of each panel

At such a high filling fraction, the film is largely a continuous film with a few dielectric voids. Consequently, the film should have a narrow absorptance band according to the EMT theory. This is indeed the situation we observe in our FDTD results, which indicate a decrease in the regions of high field intensity for longer wavelengths. Figure 9(b) shows the local-field intensities for Sample C at an incident wavelength of 400 nm. We can clearly see surface plasmons propagating away from the voids. Hence it is possible for surface plasmons to be excited by the voids. These plasmons can then propagate along the sections of the metal film that are continuous. As the wavelength is increased to 700 nm in Fig. 9(c), strong local-field enhancement is observed, giving rise to strong hot spots along the boundaries of the voids. However, as the wavelength is increased further to 1000 nm and beyond, there is significantly and progressively lower intensity enhancement in the film. This is consistent with the EMT picture, which predicts a strong local intensity en-

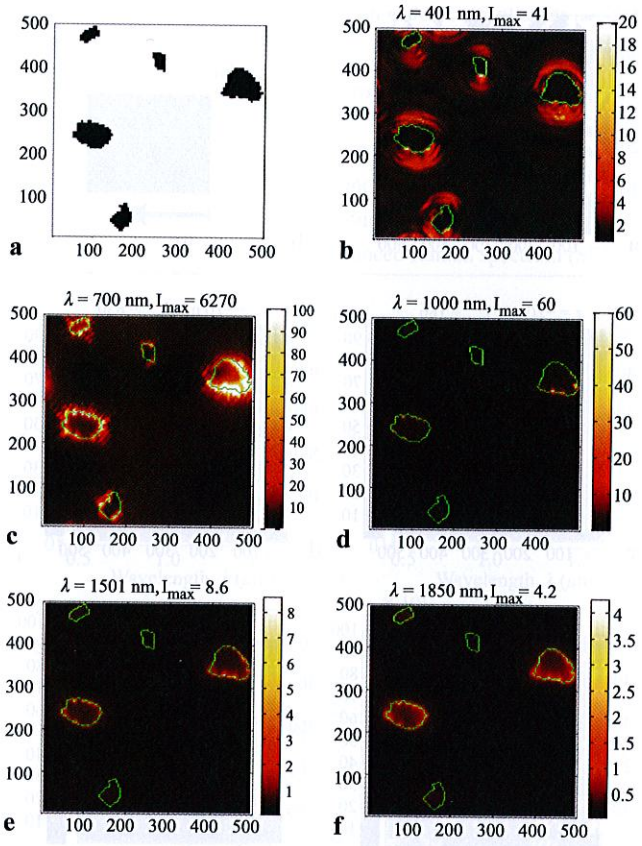

Fig. 9 (**a**) In-plane geometry of the simulated film (Sample C). (**b–f**) Local intensity maps of the film at various incident wavelengths. The intensity maps were calculated inside the glass substrate just below the film/substrate interface. The *green outlines* show the boundaries of the metal islands for reference. The maximum and minimum local intensities with respect to the incident intensity are shown in the title of each panel

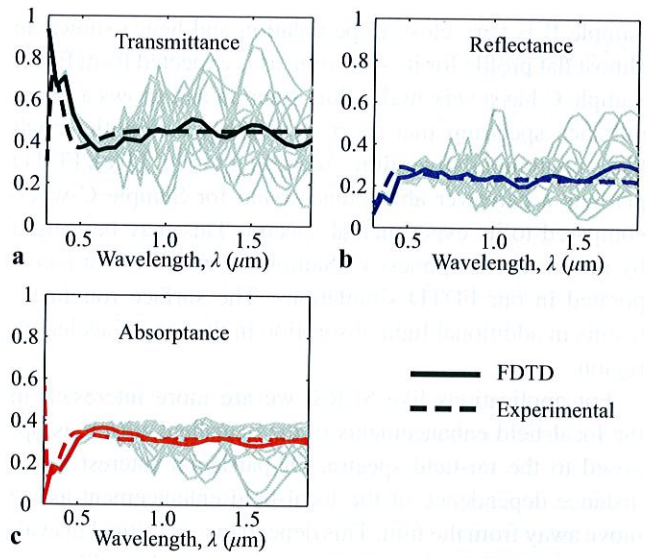

Fig. 10 The transmittance, reflectance and absorptance spectra for a 20 nm-thick metal dielectric composite with the geometry obtained from SEM images of Sample B. The results were obtained by averaging the results of 16 instances. The *light green line* shows the results for individual instances and the *solid line* shows the average. The *dashed line* shows the experimental spectra

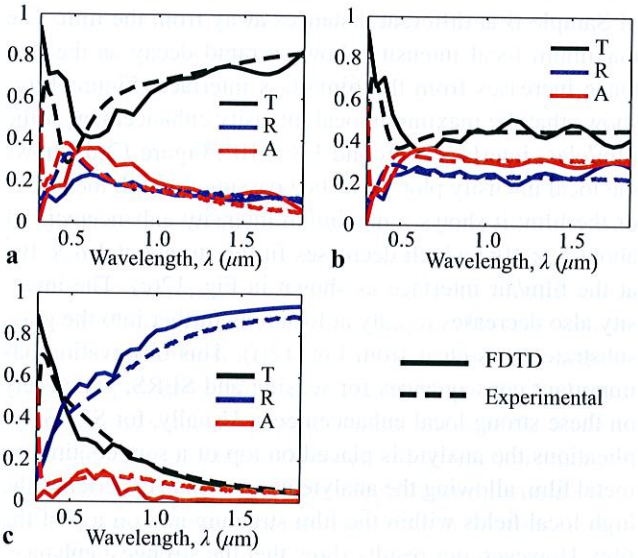

Fig. 11 The simulated and experimental transmittance, reflectance and absorptance spectra for Sample A (**a**), Sample B (**b**), and Sample C (**c**)

hancement at wavelengths within the absorptance band of the structure.

The simulation results of the individual geometries (that is, of individual SEM image sections) can vary widely from each other even if the geometries were obtained from SEM images of the same sample. Hence, in order to obtain a statistical average of the overall response of the film, we simulated a representative number of geometries for each film. The various realizations were obtained from SEM images of the film from various regions across the entire sample substrate.

Figure 10 shows the statistical average response for far-field spectra obtained for Sample B using multiple realizations of the film structure. In this case, 16 different geometries were simulated to obtain individual far-field spectral responses, and the results were averaged to obtain the mean response. In the figure, the light green lines represent the results of individual realizations, while the solid lines represent the average response of the 16 realizations. The dashed lines show the experimental spectra for Sample B. Although the individual spectra may show wide deviations, the averaged simulated spectra show very good agreement with the measured, experimental spectra.

Similar simulations were performed for Samples A and C. Figure 11 summarizes the results for the three samples under consideration. Sample A has a filling fraction of 40% and is consequently below the percolation threshold. As a result, its transmittance spectrum shows a gradual increase with increasing wavelengths. On the other hand,

Sample B is very close to percolation and hence shows an almost flat profile for its spectrum, as is expected from EMT. Sample C has a very high filling fraction and shows a transmittance spectrum that decreases with wavelength, much like a continuous silver film. According to Fig. 11(c), FDTD predicts a narrower absorptance band for Sample C when compared to its experimental spectra. This may be caused by the surface roughness of Sample C, which is not incorporated in our FDTD simulations. The surface roughness results in additional light absorption in the long-wavelength region.

For applications like SERS, we are more interested in the local-field enhancements in the near-field region as opposed to the far-field spectra. Of particular interest is the distance dependence of the local-field enhancement as we move away from the film. This dependence is critical in evaluating the SERS enhancements for large analytes like protein molecules, organic cells, viruses, and others. Intuitively, one would assume an exponential decay for the field intensities based on the fact that the highly localized hot spots are the result of modes that are evanescent in nature, i.e. modes with high transverse k-vectors. As an example, in Fig. 12 we show the intensity map of one of the geometries of Sample B at different distances away from the film. The maximum local intensity shows a rapid decay as the distance increases from the film/glass interface. Figure 12(e) shows that the maximum local intensity enhancement at the film/glass interface is around 1.8×10^4. Figure 12(d) shows the local intensity plot for a slice passing through the center of the film; it shows a maximum intensity enhancement of about 8×10^2, which decreases further to about 1.8×10^2 at the film/air interface as shown in Fig. 12(c). The intensity also decreases rapidly at locations further into the glass substrate, as is clear from Fig. 12(f). This observation has important consequences for sensing and SERS, which rely on these strong local enhancements. Usually, for SERS applications the analyte is placed on top of a semicontinuous metal film, allowing the analyte molecules to experience the high local fields within the film structure and on top of the film. However, our results show that the strongest enhancements actually occur inside the substrate, and these hot spots are not accessible by the analyte. We could significantly increase the efficiency of a SERS signal by moving the high field enhancements from the substrate region to the film and air regions. In the next section we will look in more detail at the local-field enhancements and also consider an option for achieving high field enhancements inside the film and at the film/air interface.

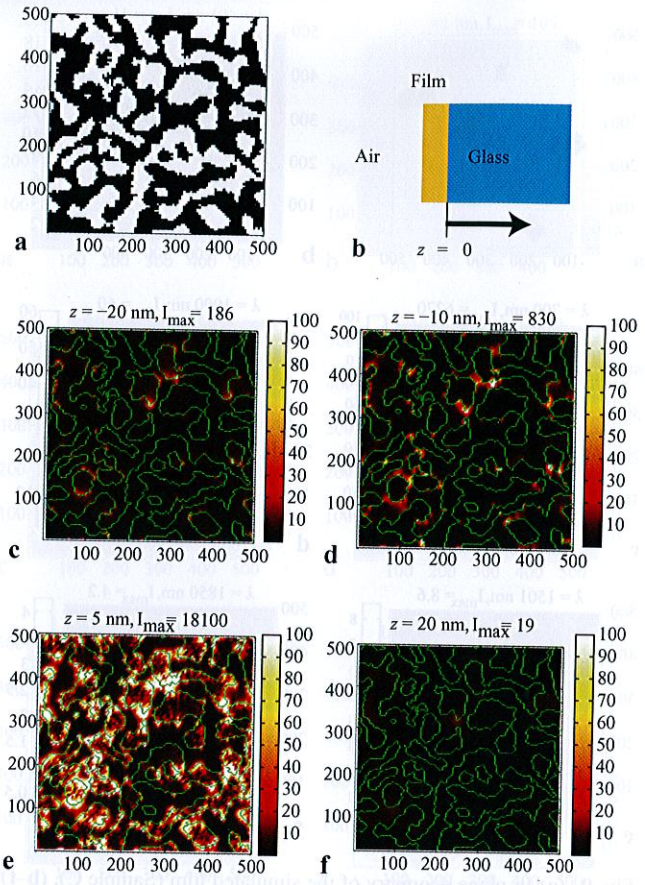

Fig. 12 **(a)** In-plane geometry of the simulated film (Sample B). **(b)** Schematic showing the z-coordinate definition for the sample. **(c–f)** Intensity maps corresponding to different values of z. The wavelength was fixed at 700 nm. The *green outlines* show the boundaries of the metal islands for reference. The value of z and the maximum and minimum local intensities with respect to the incident intensity are shown in the title of each panel

3.3 High-order field moments

In order to quantitatively study the implications of the local-field enhancement on nonlinear processes in the film, we considered the high-order field moments defined by the following equation [5]

$$M_{n,m} = \frac{\langle |E^n| E^m \rangle}{|E_0^n| E_0^m}, \tag{2}$$

where E_0 represents the incident field and E represents the local field. The angular brackets represent averaging over the entire film surface. The high-order field moments are very important parameters as they are directly related to the enhancement factors for various processes. For example, $M_{2k,m} \sim \langle E^{m+k} E^{*k} \rangle$ (where $2k = n$) corresponds to a multiphoton process where in one elementary act $m+k$ photons are created and k photons are annihilated. The complex conjugation on the second term represents the annihilation of photons. In this manner, all the high-order field moments have a corresponding multiphoton process associated with it. Table 1 lists some of the more important field moments and the associated multiphoton process. We have calculated $M_{2,0}$ and $M_{4,0}$ for the three samples (Samples A, B and C)

Table 1 Relationship between some high-order moment terms and the corresponding nonlinear processes [5]

Expression	Nonlinear process
$M_{2,2}$	Kerr optical nonlinearity
$\|M_{0,2}\|^2$	Second harmonic generation (SHG)
$\|M_{0,3}\|^2$	Third harmonic generation (THG)
$M_{4,0}$	Surface-enhanced Raman spectrum (SERS)

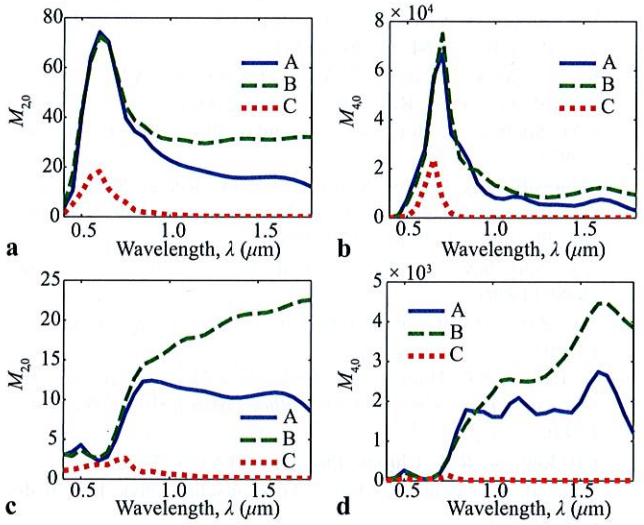

Fig. 13 High-order field moments for Samples A, B and C. (**a**) $M_{2,0}$ at the film/glass interface, (**b**) $M_{4,0}$ at the film/glass interface, (**c**) $M_{2,0}$ at the film/air interface, and (**d**) $M_{4,0}$ at the film/air interface

using our FDTD simulation results to obtain the local-field distributions. Moment $M_{2,0}$ simply corresponds to the average intensity enhancement, whereas $M_{4,0}$ is related to the enhancement in the Raman spectrum as shown in Table 1.

In Fig. 13 we plot these moments for the three samples as a function of the wavelength. The light was incident from the air side of the sample. In Fig. 13, panels (a–b) show the field moments at the film/glass interface, and panels (c–d) show the moments at the film/air interface. From these plots, it is clear that Sample B shows the highest field moments among the three samples. This is expected since Sample B is closest to the percolation threshold as seen from its far-field spectra (Fig. 2). Sample A also shows sizeable moments since it is also reasonably close to the percolation threshold. However, Sample C shows much lower moments since it is far above the percolation threshold with a metal filling fraction of 94%. Another important conclusion that can be derived from the data presented in Fig. 13 is the position dependence of these moments. Comparing the moments at the film/glass and film/air interfaces, we can see that these moments are lower at the film/air interface. For sensing applications, we need a higher moment at the film/air interface since that is where the analyte is usually located.

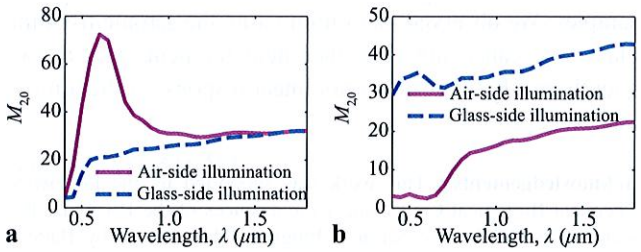

Fig. 14 High-order field moments for Sample B under different source directions. (**a**) $M_{2,0}$ at film/glass interface, (**b**) $M_{2,0}$ at film/air interface

In the above simulations, the light was incident from the air side of the sample. An obvious suggestion would be to illuminate the sample from the glass side to see if this will affect the locations of the high field moments. Since Sample B shows the highest overall moments, we compared the moments of Sample B with illumination from both sides. Figure 14 shows the results of these simulations. From the figure, we see that with glass-side illumination, the moment is lower at the film/glass interface for shorter wavelengths. As the wavelength increases, the moments at the film/glass interface converge to the same value regardless of the illumination side. At the more important film/air interface, however, glass-side illumination yields a significantly higher moment at all wavelengths.

4 Summary

In order to quantitatively study the near-field response and local-field fluctuations in semicontinuous metal films (SMFs), we performed full-wave simulations of such films using the 3D finite-difference time-domain (FDTD) method. Most of the results from FDTD show excellent agreement with the experimentally observed far-field spectra. However, there remains some discrepancy in the width of the absorptance band for samples with metal filling fractions that are significantly different from the percolation threshold. This could be the result of surface roughness in the film, which is currently not incorporated in the FDTD simulations. The effective medium theory predicts the far-field spectra of the semicontinuous metal films very well when the films are near the percolation threshold, but EMT underestimates the absorptance band of these films for filling fractions that are away from the percolation threshold. Another disadvantage of EMT is that it does not provide local-field or intensity distributions, and hence cannot describe the local fluctuations in either the electric field or the intensity. These fluctuations play a very important role in the enhancement of nonlinear processes such as SERS. In contrast, the FDTD method provides very useful insight into the local behavior of these fields. Specifically, we looked into the behavior of the high-order field moments for several semicontinuous metal film

samples. We observed that illuminating the sample from the glass side can result in higher field moments and consequently result in a stronger nonlinear response at the film/air interface.

Acknowledgements This work was supported by the Edgewood Chemical Biological Center under the auspices of the US Army Research Office Scientific Services Program administered by Battelle (Delivery Order 0030, Contract No. W911NF-07-D-0001), and in part by U.S. Army Research Office under grant number 50372-CH-MUR.

References

1. D.A.G. Bruggeman, Ann. Phys. (Leipz.) **24**, 636 (1935)
2. V.M. Shalaev, M.I. Stockman, R. Botet, Physica A **185**, 181 (1992)
3. A.K. Sarychev, R.C. McPhedran, V.M. Shalaev, Phys. Rev. B **62**, 8531 (2000)
4. V.A. Podolskiy, A.K. Sarychev, E.E. Narimanov, V.M. Shalaev, J. Opt. A, Pure Appl. Opt. **7**, S32 (2005)
5. A.K. Sarychev, V.M. Shalaev, Phys. Rep. **335**, 276 (2000)
6. U.K. Chettiar, A.V. Kildisheo, T.A. Klar, V.M. Shalaev, Opt. Express **14**, 7872 (2006)
7. M. Moskovits, Rev. Mod. Phys. **57**, 783 (1985)
8. V.P. Drachev, M.D. Thoreson, E.N. Khaliullin, V.J. Davisson, V.M. Shalaev, J. Phys. Chem. B **108**, 18046 (2004)
9. V.P. Drachev, M.D. Thoreson, V. Nashine, E.N. Khaliullin, D. Ben-Amotz, V.J. Davisson, V.M. Shalaev, J. Raman Spectrosc. **36**, 648 (2005)
10. V.P. Drachev, V.C. Nashine, M.D. Thoreson, D. Ben-Amotz, V.J. Davisson, V.M. Shalaev, Langmuir **21**, 8368 (2005)
11. K. Kneipp, Y. Wang, H. Kneipp, L.T. Perelman, I. Itzkan, R.R. Dasari, M.S. Feld, Phys. Rev. Lett. **78**, 1667 (1997)
12. M. Osawa, M. Ikeda, J. Phys. Chem. **95**, 9914 (1991)
13. A. Hartstein, J.R. Kirtley, J.C. Tsang, Phys. Rev. Lett. **45** (1980)
14. M. Osawa, in *Near-Field Optics and Surface Plasmon Polaritons*, vol. 81 (Springer, Berlin, 2001), p. 163
15. D. Enders, A. Pucci, Appl. Phys. Lett. **88**, 184104 (2006)
16. M. Westphalena, U. Kreibiga, J. Rostalskib, H. Lüthb, D. Meissner, Sol. Energy Mater. Sol. Cells **61**, 97 (2000)
17. A. Yakimov, S.R. Forrest, Appl. Phys. Lett. **80**, 1667 (2002)
18. D.A. Genov, A.K. Sarychev, V.M. Shalaev, J. Nonlinear Opt. Phys. **12**, 419 (2003)
19. P. Nyga, V.P. Drachev, M.D. Thoreson, V.M. Shalaev, Appl. Phys. B, Lasers Opt. **93**, 59 (2008)
20. S. Ducourtieux, V.A. Podolskiy, S. Gresillon, S. Buil, B. Bernini, P. Gadenne, A.C. Boccara, J.C. Rivoal, W.D. Bragg, K. Banerjee, V.P. Safonov, V.P. Drachev, Z.C. Ying, A.K. Sarychev, V.M. Shalaev, Phys. Rev. B **64**, 165403 (2001)
21. K. Seal, M.A. Nelson, Z.C. Ying, D.A. Genov, A.K. Sarychev, V.M. Shalaev, Phys. Rev. B **67**, 035318 (2003)
22. V.M. Shalaev, R. Botet, A.V. Butenko, Phys. Rev. B **48**, 6662 (1993)
23. S. Gresillon, L. Aigouy, A.C. Boccara, J.C. Rivoal, X. Quelin, C. Desmarest, P. Gadenne, V.A. Shubin, A.K. Sarychev, V.M. Shalaev, Phys. Rev. Lett. **82**, 4520 (1999)
24. A.K. Sarychev, V.A. Shubin, V.M. Shalaev, Phys. Rev. B **60**, 16389 (1999)
25. X.C. Zeng, D.J. Bergman, P.M. Hui, D. Stroud, Phys. Rev. B **38**, 10970 (1988)
26. A. Taflove, S.C. Hagness, *Computational Electromagnetics: The Finite Difference Time Domain Method* (Artech House, Norwood, 2000)
27. P.B. Johnson, R.W. Christy, Phys. Rev. B **6** (1972)
28. Y. Yagil, P. Gadenne, C. Julien, G. Deutscher, Phys. Rev. B **46**, 2503 (1992)
29. V.M. Shalaev, *Optical Properties of Random Media* (Springer, Berlin, 2002)
30. A.K. Sarychev, D.J. Bergman, Y. Yagil, Phys. Rev. B **51**, 5366 (1995)
31. U. Kreibig, M. Vollmer, *Optical Properties of Metal Clusters* (Springer, Berlin, 1995)